Akira Yamaguchi[1]
e-mail: yamaguchi@nucl.eng.osaka-u.ac.jp

Takashi Takata
e-mail: takata_t@nucl.eng.osaka-u.ac.jp

Graduate School of Engineering,
Osaka University,
2-1, Yamada, Suita,
Osaka 565-0871, Japan

Hiroyuki Ohshima
Japan Atomic Energy Agency,
4002, Narita, O-arai,
Ibaraki 311-1393, Japan
e-mail: ohshima.hiroyuki@jaea.go.jp

Yoshitaka Kohara
Graduate School of Engineering,
Osaka University,
2-1, Yamada, Suita,
Osaka 565-0871, Japan
e-mail: kohara_y@qe.see.eng.osaka-u.ac.jp

Yoshihiro Deguchi
Mitsubishi Heavy Industry,
5-717-1, Fukahori-machi,
Nagasaki 851-0392, Japan
e-mail: yoshihiro_deguchi@mhi.co.jp

Numerical Prediction and Optimization of Depressurized Sodium-Water Reaction Experiment With Counterflow Diffusion Flame

Sodium-water reaction (SWR) is a design basis accident of a sodium-cooled fast reactor (SFR). A breach of the heat transfer tube in a steam generator results in contact of liquid sodium with water. Typical phenomenon is that the pressurized water blows off, vaporizes, and mixes with the liquid sodium. It is necessary to quantify the SWR phenomena in the safety evaluation of the SFR system. In this paper, a new computer program has been developed and the SWR in a counterflow diffusion flame is studied by a numerical simulation and an experiment. The experiment is designed based on the numerical simulation so that the stable reaction flame is maintained for a long time and physical and chemical quantities are measured. From the comparison of the analysis and the experiment, there exist discrepancies that may be caused by the assumptions of the chemical reaction. Hence, a new experiment is proposed to enhance the measurement accuracy and to investigate the reason of the disagreement. The authors propose a depressurized experiment and show the preliminary result of the experiment. It is found that a stable chemical reaction flame is formed. With the depressurization, it is expected that the flame location can be controlled and the reaction region becomes thicker because of decrease in the reactant gas density. [DOI: 10.1115/1.3043822]

1 Introduction

1.1 Background and Purpose. In a sodium-cooled fast reactor (SFR), liquid sodium is used as the heat transfer fluid to carry the energy from the reactor core to the steam generation (SG) system. The liquid sodium has an excellent heat transport capability and a large safety margin to the boiling point (1153 K) at the atmospheric pressure. On the other hand, it has chemical reactivity in contact with water vapor. One of the design basis accidents of the SFR is the water leakage into the liquid sodium through a heat transfer tube of SGs, i.e., a sodium-water reaction (SWR).

Consequently, coupled phenomena of the chemical reaction and the thermal-hydraulics of sodium and water vapor are of importance from the safety viewpoint. Large-scale experiment series of SWR were performed in Japan [1]. However, the SWR phenomena are generally complex and the experimental measurement technology is not well matured. Therefore, a numerical simulation is used to investigate the coupled phenomena and local quantities such as mass concentrations, flow velocities, and temperatures.

According to Takata et al. [2], two chemical reaction types are considered, i.e., a surface reaction and a gas-phase reaction. In the initial phase of the SG tube failure accident, the temperature is well below the sodium boiling point and little sodium vapor exists. Therefore, the water vapor and the liquid sodium react at the gas-liquid interface. It is the surface reaction that occurs at the liquid sodium surface. Subsequently, the liquid sodium is heated up by the exothermic reaction. At this stage, sodium vaporizes and the sodium vapor and the water vapor encounter. It results in the gas-phase reaction. In general, most of the sodium remains a liquid phase because of a large amount of the liquid sodium inventory.

This paper deals with a numerical simulation and a SWR experiment in the gas phase. It is advantageous to study the gas-phase reaction to understand the characteristics of the SWR. In the gas-phase reaction, one can calculate the spatial distributions of the reactants and product including airborne particulates as well as a temperature by solving conservation equations. For validating the numerical method, a counterflow diffusion flame experiment was performed [3]. Numerically obtained spatial distributions of quantities are compared with the experimental measurement. According to the comparison, discrepancies are found between the experiment and the analysis. Here a new experiment is proposed to enhance the measurement accuracy of the chemical and thermal quantities, that is, an experiment in depressurized conditions.

1.2 Sketch of SWR. The pressure of the water side is approximately 17 MPa and that of the sodium side is 0.2 MPa. The temperatures in the sodium side are 625 K and 743 K for the cold leg and the hot leg, respectively, of the heat transport system. The sodium is in liquid phase because the boiling temperature is greater than the system temperature by 500 K. A breach of a heat transfer tube in the SG results in contact of the liquid sodium with the water. Therefore, sudden influx of the water and steam into the liquid sodium takes place. The water changes into the vapor phase by sudden depressurization in quite a short time. Typical phenomenon is that the pressurized water and steam blow off and mix with the liquid sodium where many heat transfer tubes exist. At

[1]Corresponding author.

Manuscript received August 12, 2008; final manuscript received August 22, 2008; published online January 6, 2009. Review conducted by Dilip R. Ballal. Paper presented at the 16th International Conference on Nuclear Engineering (ICONE16), Orlando, FL, May 12–15, 2008.

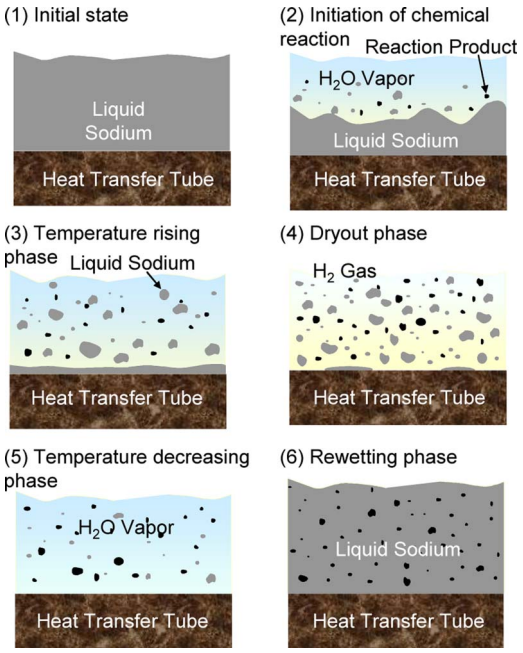

Fig. 1 Sketch of the sodium-water reaction phases

the interface of the liquid sodium and the water vapor, the SWR takes place and reaction heat and reaction products, i.e., sodium hydroxide and hydrogen, mostly are generated.

A sketch of the reaction zone around the tube surface is shown in Fig. 1. At the interface of the bulk sodium and the water vapor jet, the relative velocity is large. Hence it is reasonable to consider that liquid sodium droplets are entrained into the water vapor flow. In the initial phase, the tube is surrounded by the liquid sodium as shown in Fig. 1(1). When the water vapor flows into the liquid sodium and reaches the tube surface, the water vapor pushes the liquid sodium aside. But liquid film remains on the tube surface (Fig. 1(2)). In this phase, the SWR takes place and the region is heated up and sodium hydroxide is generated at the liquid sodium surface or in the gas phase as aerosols. As the reaction proceeds and the temperature increases, the liquid film becomes thinner (Fig. 1(3)) and comes to the dryout of the tube surface (Fig. 1(4)). In this situation, the sodium runs out and the SWR goes down.

In safety consideration, what we are interested in is the tube temperature in the temperature rising phase and the dryout phase. As mentioned above, the reaction is dominant near the interface of the water vapor and the bulk liquid sodium. As the reaction proceeds, the region is covered with the reaction product hydrogen gas (see Fig. 1(4)). It is a mechanism that mitigates the temperature increase. Subsequently, the water vapor replaces the hydrogen and the temperature begins to decrease if the water leakage continues (Fig. 1(5)). There may be still a small amount of liquid droplets of sodium since the ejecting water vapor entrains the liquid sodium droplets and carry them to the zone. The SWR continues, but it is mild and the temperature transient is benign. After the water leakage ceases, liquid sodium flows in again and the tubes are cooled down (Fig. 1(6)). At this stage, the SWR process is terminated.

2 Computational Model

In the computer program, Navier–Stokes equations and chemical reaction equations are solved interactively. In addition, a dynamic equation of airborne particulates is coupled with the basic equations of thermal-hydraulics. A source of the particulates is the chemical reaction products, i.e., sodium hydroxide and sodium oxide. Details of the computational models are given in Ref. [3]. In this section the authors describe the governing equations and the computational modeling briefly.

2.1 Governing Equations. Governing equations for thermal-hydraulics are described. Taking the Reynolds average of the conservation equations, one obtains time-averaged equations as follows:

For mass conservation equation,

$$\frac{\partial \rho}{\partial t} + \mathrm{div}\ \rho \bar{\mathbf{u}} = \sum_k S_k \tag{1}$$

For momentum conservation equation,

$$\frac{D\bar{u}_i}{Dt} = -\frac{1}{\rho}\mathrm{grad}\ \bar{p} + \mathrm{div}(\nu\ \mathrm{grad}\ \bar{u}_i - \overline{u_i' u_j'}) + g_i - \frac{\bar{u}_i}{\rho}\sum_k S_k \tag{2}$$

For conservation equation of chemical species,

$$\frac{D\rho Y_k}{Dt} = \mathrm{div}(\rho D_k\ \mathrm{grad}\ Y_k) + S_k \tag{3}$$

For energy conservation equation,

$$\frac{D(\rho C_p \bar{T})}{Dt} = \mathrm{div}(\lambda\ \mathrm{grad}\ \bar{T} - \rho C_p \overline{u_i' T'}) + F + Q_R \tag{4}$$

The explanation of the variables is given in the Nomenclature. $\bar{\cdot}$ and $\cdot'$ indicate the time average and fluctuating parts of a quantity, e.g., $u_i = \bar{u}_i + u_i'$. $S_k = \partial(\rho Y_k)/\partial t$ is the production term of species k by the chemical reaction.

Assuming the gradient-diffusion hypothesis, the Reynolds stress $\overline{u_i' u_j'}$ and the turbulent heat flux $\overline{u_i' T'}$ are defined using the turbulent viscosity and the turbulent thermal diffusivity. The equations for the turbulence energy and the energy dissipation ratio are based on those for the low-Reynolds number two-equation model proposed by Yang and Shih [4], which is a variation of Jones and Launder's model [5] and describes the near-wall effect. A zero-equation model is used with regard to the temperature field. According to the recommendation by Nagano and Tsuji [6], Wassel–Catton equation is used for the turbulent Prandtl number. The correlations and the parameters appearing in the turbulence model are given by Yang and Shih [4] and Nagano and Tsuji [6].

2.2 Aerosol Dynamics. For evaluating the aerosol behavior, the evolution of the size distribution is calculated by solving the following general dynamics equation:

$$\frac{\partial n(v)}{\partial t} + \mathrm{div}\left(\frac{n(v)}{C_u(v)}\mathbf{u}\right) + \mathrm{div}(n(v)\mathbf{U}) = \frac{1}{2}\int_0^v n(v')n(v-v')\beta(v', v-v')dv' - n(v)\times\int_0^\infty n(v')\beta(v, v')dv' + S(v) \tag{5}$$

Aerosols are transferred in a thermal-hydraulic field by convection, diffusion, thermophoresis, diffusiophoresis, and gravity fallout. In the transfer processes of the aerosol mass, coagulation and sedimentation are major mechanisms of the change in the aerosol size distribution. The Brownian movement, the velocity difference of two aerosol particles, and the turbulence are the mechanisms for the coagulation. Gelbard and Seinfeld [7] gave details on the modeling of the coagulation process, which is used in the present model.

The second term in the left hand side of Eq. (5) is the advection term due to the gas velocity. In this equation, $C_u(v)$ is the Cunningham correction factor to explain slip effect for smaller diameter particles than the mean free path of the gas. The third term in

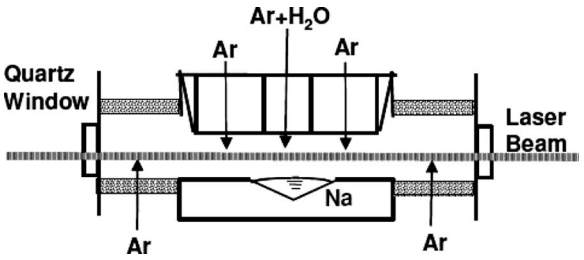

Fig. 2 Sodium-water counterflow diffusion flame experiment

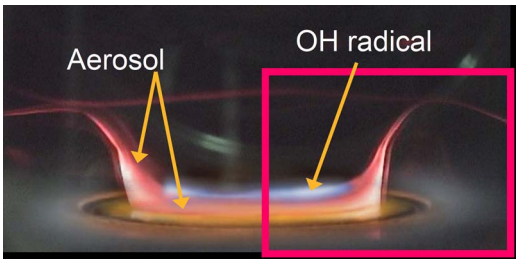

Fig. 3 Visualization of sodium-water reaction

the left side of Eq. (5) represents the mass transfer caused by applied forces to the aerosols. **U** is the terminal velocity vector of a particle, which is expressed as

$$\mathbf{U} = \mathbf{U}_{\text{dif}} + \mathbf{U}_g + \mathbf{U}_{tp} + \mathbf{U}_{dp} \tag{6}$$

where the velocities with subscripts dif, *g*, *tp*, and *dp* are contributions from the Brownian diffusion, the gravity, the thermophoresis, and the diffusiophoresis forces, respectively.

The aerosol source term is obtained based on the reaction rate evaluated by the chemical reaction model. One assumes that the statistical distribution of the primary aerosol diameter follows a lognormal distribution. The volume fraction of the aerosols is little and the interaction of the aerosols and the air flow can be neglected in the gas dynamics calculation.

2.3 Radiation Heat Transfer. We assume one-dimensional radiation heat transfer because we are dealing with the pool surface phenomena. Using the gas temperature T_i in the *i*th computational cell numbered from the pool surface in the vertical direction, one obtains the following equations regarding the volumetric heat generation rate Q_i of an individual cell:

$$q_i = Q_i L_i = \varepsilon_i G_p \prod_{j=1}^{i-1} (1-\varepsilon_j) + \varepsilon_i \sum_{j \neq i} \left\{ \varepsilon_j \sigma T_j^4 \prod_{k=i+1}^{j-1} (1-\varepsilon_k) \right\} - 2\varepsilon_i \sigma T_i^4 \tag{7}$$

$$G_p = \varepsilon_p \sigma T_p^4 + (1-\varepsilon_p)\sigma \sum_{j=1}^{n} \varepsilon_j T_j^4 \prod_{k=1}^{j-1} (1-\varepsilon_k) \tag{8}$$

Here L_i and T_i are the cell size and the local gas temperature, respectively, in the *i*th computational cell. G_p in the first term of the right hand side of Eq. (7) is the leaving flux from the pool surface and is given by Eq. (8). The pool surface emissivity is influenced by the surface conditions and ε_p=0.65 is assumed according to the measurement by Hashiguchi et al. [8].

The total gas mixture emissivity including aerosols is evaluated by Modak's [9] radiative property model and is applied to each computational cell.

$$\varepsilon_i = \varepsilon_a + \varepsilon_{\text{gas}} - \varepsilon_a \varepsilon_{\text{gas}} \tag{9}$$

where ε_{gas} and ε_a are the gas and the aerosol emissivity, respectively. ε_{gas} is calculated from the emissivity of the individual nontransparent gas with a correction for the overlapping of absorption bands from different gases. It can be assumed that the emissivity is equal to the absorptivity for aerosols. ε_a is evaluated according to Felske and Tien [10] as a function of the local value of gas temperature, the mass density, and the volume fraction of the aerosols.

3 SWR Experiment and Code Validation

3.1 SWR in Counterflow Diffusion Flame. To understand the SWR phenomena and to validate the numerical simulation method, a counterflow laminar combustion experiment of SWR was performed by Yamaguchi et al. [3]. Figure 2 shows the schematics of the sodium-water counterflow experiment.

The outline of the experiment is as follows. A liquid sodium pool is heated up to 800 K (less than the boiling point by 253 K) so that the sodium evaporates slowly. Through the nozzle above the liquid pool surface, water vapor diluted to 0.7 vol % by argon gas flows out toward the sodium pool surface. A strainer is installed at the exit of the mixture gas flow to provide flat velocity distribution. Hence a counterflow diffusion flame is formed between the pool surface and the flow nozzle. The reaction zone exists in between the sodium pool and the strainer. It is important to keep the water vapor density at a very low value for visualizing the flame zone. Otherwise, we cannot see the experimental cell inside because it is filled with white smoke (reaction product aerosol of sodium hydroxide).

Figure 3 is the photo of the reaction zone as well as the aerosol mass concentration taken in the experiment. The sodium pool diameter is 0.03 m. In the experiment, the existence of OH radical is measured by the laser-induced fluorescence (LIF) technique. Bright region above the pool shows the OH radical fluorescence intensity. In the reaction, the water molecule decomposes first of all to produce OH radical, which bonds with the Na molecule. Therefore, the chemical reaction takes place in the region where OH fluorescence intensity is high. The region is located 2 mm from the liquid sodium pool surface. The thickness of the reaction zone is approximately 1 mm.

The aerosol concentration is visualized by the scattering of the laser beam from the aerosol particles. We can see the red light emission from the levitating aerosols. The aerosol existing area is like a "crown" shape. This state is maintained for a long time duration and is very stable. Figure 4 shows the numerical results of the aerosol mass concentration. The numerical simulation is performed in two-dimensional geometry assuming axis symmetry.

In Figs. 3 and 4, we can see that the aerosol is dense above the liquid sodium pool. They move upward at the pool edge and are removed from the reaction zone. The flow field is in a mixed condition of forced and natural convections. Then the flow field and aerosol distributions are influenced by the temperature distribution as well. Also we can see that the stable reaction flame is established. Since the saturated vapor pressure of sodium is very low, the flame location tends to adhere to the pool surface. It is important to lift the flame off the pool surface for measurements with an enhanced accuracy.

However, trial-and-error process by a series of experiments is not practical to find out the best solution. Thus, the experimental condition (the geometry of the cell, boundary condition of flow

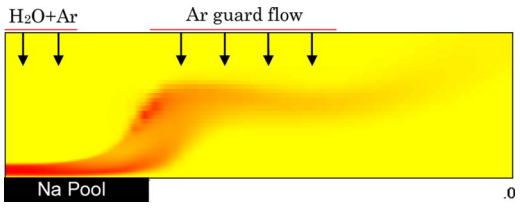

Fig. 4 Aerosol mass concentration

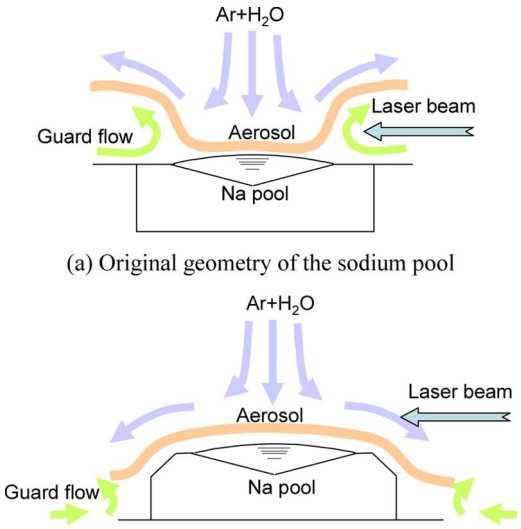

Fig. 5 Modification of the sodium pool: (*a*) original geometry of the sodium pool and (*b*) modified geometry of the sodium pool

velocities, and temperatures) is optimized based on numerical simulations. To lift the flame up, double guard flows at different radial coordinates are used as shown in Fig. 2. One is an inner downward argon flow surrounding the H_2O+Ar flow. The inner guard flow is used to confine the water vapor in the above-pool region. Another is an outer upward argon flow located at the peripheral of the experiment cell. The outer guard flow plays an important role of lifting up the reaction flame.

With this process, the flow and the temperature fields surrounding the flame are adjusted so that the flame zone is detached away from the pool surface and the reaction products are removed from the reaction zone. The combination of the two guard flows is found to be appropriate to establish the optimal flow field for continuous chemical reaction and clear visualization and measurement. From the comparison of the numerical simulation and the experimental observation, the performance of the present simulation is satisfactorily accurate and the optimization procedure of the flow and temperature and the experimental design works well. The dilution of water vapor and two guard flows enable sufficiently long duration time of the reaction. Accordingly one can extend the reaction duration time as long as 1 h and achieve steady state reaction flame, and no change in the liquid sodium level is observed during 5 min measurement. It is long enough for the laser measurement and visualization of the thermal-hydraulic field.

3.2 Modification of Sodium Pool Geometry. It is noted from Fig. 3 that the reaction zone is closed to the pool surface and a dense aerosol region exists above the sodium pool peripheral. The laser beam is irradiated in the lateral direction permeating through the quartz window as shown in Fig. 2. Therefore there is a concern that the thick aerosol region may deteriorate the transparency or visibility from the window. Thus a modification of the geometry of the edge of the sodium pool is considered.

Figure 5(*a*) shows the original geometry and schematic flow pattern as well. A qualitative explanation of the flow field is given in the following. The temperature of the outer guard flow is kept lower than the inner guard flow and the upward flow velocity is small. Therefore the outer guard flow direction turns to horizontal toward the pool center. Then it turns upward flow at the peripheral of the sodium pool. The upward guard flow is useful to remove the reaction product aerosol to the upper right of the figure and to make the flame visible. However, the aerosol region is stretched

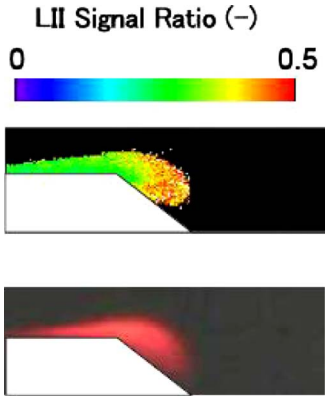

Fig. 6 Photo of the laser scattering by aerosols (bottom) and relative size of the aerosols measured by LII (top)

upward at the pool peripheral, which may deteriorate the side view. Therefore, the edge of the pool is cut off as shown in Fig. 5(*b*) and the flow pattern is changed by adjusting the water vapor flow and the guard flow conditions. We expect the aerosol distribution as in Fig. 5(*b*) and better visibility from the window.

The bottom of Fig. 6 is the photo of the aerosols in the experiment with the modified geometry in Fig. 5(*b*). The water vapor concentration is 1.6 vol % and $Ar+H_2O$ flow velocity is 0.12 m/s. It is seen that the upward stretching of the aerosol at the pool peripheral is suppressed and is similar to what the authors expected in advance. The numerical simulation results of the aerosol density for the same condition as the experiment are shown in Fig. 7. It can be said that the aerosol distribution is in agreement with the experiment although quantitative comparisons are necessary in the future.

The laser-induced incandescence (LII) measurement result is shown in the top of Fig. 6. The LII signal intensity was measured twice at 200 ns and 300 ns after the laser irradiation. The ratio of the two LII signals is shown in Fig. 6 (top). The aerosol particle temperature rises by the laser irradiation followed by the cooling down as time goes. Hence the ratio of the two LII signal intensities lies between zero and unity. Large particles with high thermal capacity are cooled down slowly and the LII signal ratio is close to unity. On the other hand, small particles with a little mass heat capacity are cooled down fast and the LII signal ratio approaches to zero. Therefore, the LII signal ratio corresponds to the particle diameter. Although quantitative measurement is not performed yet, we understand that the particle grows and the size becomes larger in the pool peripheral from Fig. 6.

In the numerical simulation, the diameter of the incipient aerosol generated by the chemical reaction is assumed to be 0.5 μm. The aerosol diameter is divided into groups from 0.5 μm to 100 μm in lognormal scale. A small aerosol is subjected to the forces dominant in a small scale such as thermophoresis and diffusion [11]. Being driven by the forces, they move upward or downward before they coagulate to grow larger. Large aerosols follow the macroscopic phenomena such as a gas flow.

Figure 8 shows the LIF measurement result and the OH radical

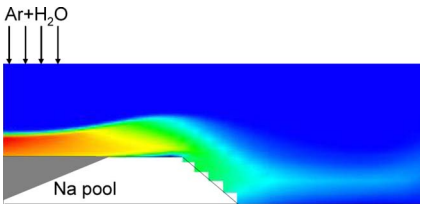

Fig. 7 Mass concentration of aerosols

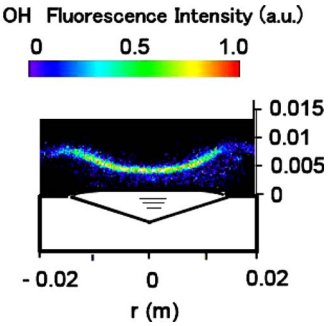

Fig. 8 Concentration of the OH radical measured by LIF

concentration in arbitrary unit. We see that the reaction zone exists at 4 mm above the pool surface at the pool center. If the existence of the OH radical corresponds to the reaction region, the reaction region lies above the dense aerosols. It is noted that the reaction zone is axisymmetric, which justifies the assumption in the numerical simulation.

Numerical results of the mass concentration distribution of the sodium and the water vapor along the vertical axis at the pool center are shown in Fig. 9 to investigate the chemical reaction and the mass concentration in the reaction zone. The solid lines indicate the computational results and the symbols indicate the experimental measurements. From the simulation results, the reaction flame locates at 2 mm distant from the pool surface, where their mass concentrations approach zero. No sodium vapor exists beyond the combustion flame and no water vapor below it as an infinite reaction rate or a flame sheet concept is assumed.

On the contrary, in the measurement the sodium vapor and the water vapor are almost consumed and disappear at 3 mm from the pool surface. There is a discrepancy between the experiment and the numerical simulation in the flame location. From Fig. 8, the OH radical locates at 4 mm above the pool, which is more consistent with the experimental results in Fig. 9. Further investigation is needed regarding the assumption of chemical reaction rate constant, the reaction process, and/or the reaction products.

3.3 Proposal of Depressurized Experiment. To investigate the reason of the discrepancies between the analysis and the experiment mentioned in Sec. 3.2, the authors propose a depressurized experiment. We expect that the flame moves upward and the reaction region becomes thicker because of the decrease in the reactant gas density in the depressurized conditions. Therefore, the thermal-hydraulic and chemical quantities can be measured with higher accuracy.

The flame location is influenced by the relationship of the water and sodium mass fluxes. To lift up the flame location above the pool surface, one needs to either increase the sodium mass flux and/or decrease the water vapor mass flux. With the depressurization, the sodium evaporation is enhanced and the sodium mass flux increases without ascending the pool temperature by improving the capacity of the heating unit. Current pool temperature condition (800 K) is consistent with the actual situation in which the design temperature ranges from 625 K to 743 K. It is easy to control the water vapor mass flux by changing the approaching flow velocity and the water vapor concentration. Another advantage is that the gas density is decreased. The depressurization will decrease the frequency of water and sodium molecular collision. It will enlarge the reaction region.

Table 1 Computational conditions

	Pressure (kPa)	Velocity (m/s)	Water vapor (vol %)
Case 0	100	0.12	2.7
Case 1	25	0.12	2.7
Case 2	25	0.06	5.4

The authors performed sensitivity analyses to decide the most appropriate pressure and the experimental conditions. The minimum pressure is decided to be 25 kPa considering the practicability of the experiment. Two analyses are shown in comparison with the ambient pressure (100 kPa) case designated as Case 0. In Case 0 and Case 1, the water vapor concentration is assumed to be 2.7 vol % and the flow velocity is 0.12 m/s. They are changed to 5.4 vol % and 0.06 m/s in Case 2. In the three cases, the water vapor mass flux is the same at the nozzle. The computational conditions are summarized in Table 1.

Figure 10 shows the sodium and water vapor densities as a function of the distance from the pool surface. The flame location lies around 3 mm from the pool surface in Case 1 and Case 2 while the flame location is below 1 mm in Case 0. Figure 11 shows the chemical reaction product concentration. Below the reaction flame is sodium-rich and Na_2O is the dominant reaction product. On the other hand, above the flame is water-vapor-rich and the NaOH is the dominant constituent. In the experiment, the constituent will be measured, which gives important information and insight as well as the validation data on the chemical reaction model.

We have little information on the reaction rate constant and fundamental reactions. In the present simulation, chemical equivalence model is used that assumes infinite reaction rate constant. Therefore, with this modeling, the thickness of the reaction zone is infinitely small. The expansion of the reaction zone is determined by the reaction rate constant and mobility of the reactants.

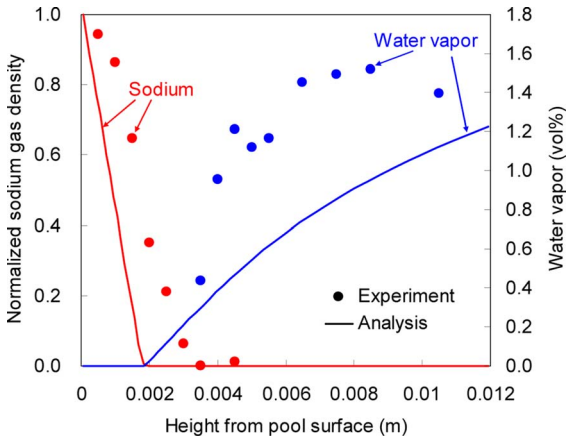

Fig. 9 Sodium and water vapor mass concentrations

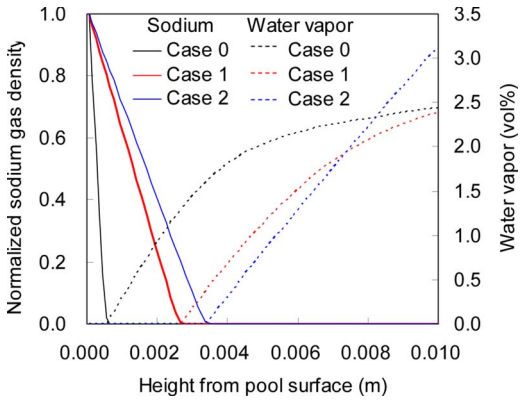

Fig. 10 Velocity vector above the pool surface

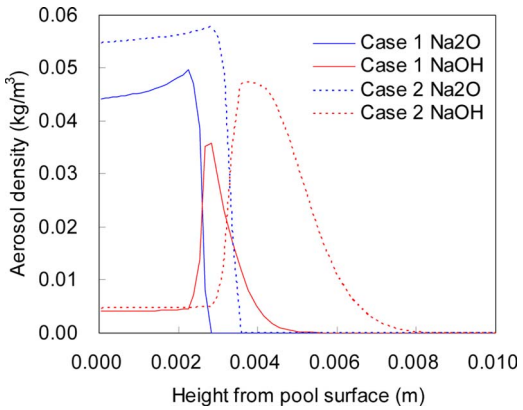

Fig. 11 Instantaneous temperature distribution

If we observe the experimental results carefully and interpret them in comparison with the numerical simulation, we may estimate the rate constant.

Figure 12 shows the aerosol mass density contour calculation. It is clear that the depressurization of the experimental cell lifts up the reaction flame, which facilitates the laser measurement from the side window.

It is noteworthy that the reaction zone where the OH radical exists is located above the aerosol (see Figs. 3, 6, and 8). Also, the existence of the OH radical has been proven. An assumption that we employ is that the chemical reaction rate is infinite, i.e., chemical equilibrium. As in Fig. 9, the water vapor and sodium vapor disappear at a flame plane with no thickness in the numerical simulation. On the other hand, the thickness of the OH radical seems to be an order of 1 mm as in Fig. 8. Further investigation is necessary by measuring the reaction zone thickness and investigating the relationship of the thickness and flow velocity or mass flux. With the information, the characteristic time of the convection flow and the chemical reaction will be quantified.

Although the depressurized experiment is currently ongoing, a preliminary result is shown in Fig. 13. The experimental condition is almost the same as Case 2 and the pressure is 24 kPa. In the photograph, we see the reacting region where the laser beam is scattered by the reaction products. The flame location is distant

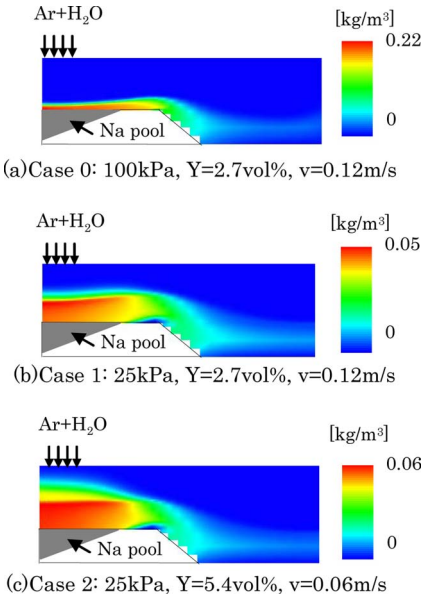

Fig. 12 Aerosol mass density for three cases

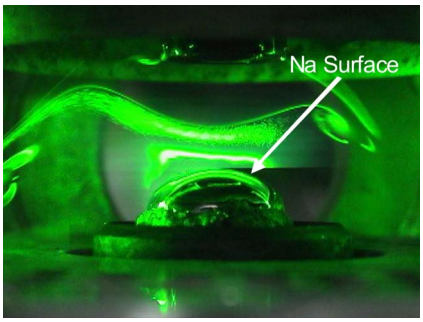

Fig. 13 Preliminary experimental result

from the sodium surface by approximately 5 mm. In the future, the authors expect quantitative measurement to be performed and the sodium-water reaction to be understood.

4 Conclusions

In this paper, a new computer program has been developed for the gas-phase reaction of the SWR. A counterflow diffusion flame is studied by a numerical simulation and an experiment. The experimental conditions are decided with the numerical simulation so that the stable reaction flame is maintained for a long time and physical and chemical quantities are measured. From the comparison of the analysis and the experiment, there exist discrepancies of the mass concentration distributions and the location of the flame. It may be caused by the assumptions of the chemical reaction model. Therefore, a new experiment is proposed to enhance the measurement accuracy and to investigate and explain the reason of the disagreement. The authors propose a depressurized experiment. We expect that the flame moves upward and the reaction region becomes thicker because of the decrease in the reactant gas density in depressurized conditions. It is expected based on the simulation that the experiment cell is depressurized to 25 kPa, the stable and thick reaction flame is generated, and the optic measurement is facilitated. Although the SWR is a complex phenomenon, the numerical simulation is useful and helpful to design an experiment to perform basic experiment. At the same time, information obtained from the experiment is useful to establish the modeling for the safety analysis code.

Nomenclature

C_p = specific heat
C_u = Cunningham correction factor
D_k = diffusion coefficient
F = heat transferred by gas diffusion
g_i = ith component of the gravity vector
k = identifier of chemical species
$n(v)$ = aerosol number density with its volume v
p = pressure
Q_R = radiation heat transfer per unit volume
S_k = mass production per unit volume
S = aerosol production rate
T = temperature
t = time
$\mathbf{u}$ = velocity vector
$\mathbf{U}$ = terminal velocity vector of the particle
u_i = ith component of the velocity vector
Y_k = molar mass density
β = aerosol coagulation rate
ε = emissivity
λ = thermal conductivity
v = kinetic viscosity
ρ = density
σ = Stephan–Boltzmann constant

References

[1] Tanabe, H., and Wachi, E., 1990, "Review on Steam Generator Tube Failure Propagation Study in Japan," *Proceedings of the IAEA/IWGFR Specialists' Meeting on Steam Generator Failure and Failure Propagation*, Aix-en Provence, France, pp. 33–35.

[2] Takata, T., Yamaguchi, A., Fukuzawa, K., and Matsubara, K., 2005, "Numerical Methodology of Sodium-Water Reaction With Multi-Phase Flow Analysis," Nucl. Sci. Eng., **150**, pp. 221–236.

[3] Yamaguchi, A., Takata, T., Ohshima, H., and Suda, K., 2006, "Sodium-Water Reaction and Thermal Hydraulics or Gas-Liquid Interface: Numerical Interpretation of Experimental Observation," *Proceedings of the 14th International Conference on Nuclear Engineering*, Miami, FL, Jul. 17–20, Paper No. ICONE14–89615.

[4] Yang, Z., and Shih, T. H., 1993, "New Time Scale Based k-e Model for Nearwall Turbulence," AIAA J., **31**, pp. 1191–1198.

[5] Jones, W. P., and Launder, B. E., 1972, "Low-Reynolds Number Phenomena With Two-Equation Model of Turbulence," Int. J. Heat Mass Transfer, **15**, pp. 301–314.

[6] Nagano, Y., and Tsuji, T., 1995, *Analysis of Turbulent Flows*, Computational Fluid Dynamics Series 3, H. Miyata, ed., University of Tokyo Press, Tokyo, p. 236.

[7] Gelbard, F., and Seinfeld, J. H., 1980, "Simulation of Multicomponent Aerosol Dynamics," J. Colloid Interface Sci., **78**(2), pp. 485–501.

[8] Hashiguchi, I., 1978, preprints 1978 Annual Meeting, Atomic Energy Society of Japan, Tokyo, Paper No. A55, in Japanese.

[9] Modak, A. T., 1979, "Radiation From Products of Combustion," Fire Research, **1**, pp. 339–361.

[10] Felske, J. D., and Tien, C. L., 1973, "Calculation of the Emissivity of Luminous Flames," Combust. Sci. Technol., **7**, pp. 25–31.

[11] Yamaguchi, A., and Tajima, Y., 2003, "Numerical Simulation of Non-Premixed Diffusion Flame and Reaction Product Aerosol Behavior in Liquid Metal Pool Combustion," J. Nucl. Sci. Technol., **40**(2), pp. 93–103.